Nanoscale

PAPER

View Article Online
View Journal | View Issue

Cite this: *Nanoscale*, 2024, **16**, 21128

Fabrication of palladium-enriched metallic structures by direct focused He^+ and Ne^+ beam nanowriting from organometallic thin films: a comparison with Ga^+ and e^- beams†

Lucía Herrer, [a] Alba Salvador-Porroche, [a] Gregor Hlawacek, [b] Pilar Cea [a,c] and José María De Teresa *[a]

A direct nanowriting procedure using helium- and neon-focused ion beams and spin-coated organometallic thin films is introduced and applied to the fabrication of Pd-enriched metallic structures in a single lithography step. This process presents significant advantages over multi-step resist-based lithography and focused beam-induced deposition using gaseous precursors, such as its simplicity and speed, respectively. The optimized process leads to Pd-rich structures with low electrical resistivity values of 141 and 152 μΩ cm under Ne^+ or He^+ fluences of 1000 and 5000 μC cm^{-2}, respectively. These resistivity values correlate well with compositional and microstructural studies, indicating a high Pd metallic content in a dense structure with a few-nm grain size. The obtained results are compared to similar structures fabricated by direct electron and gallium beam nanowriting, demonstrating the full potential of nanopatterned Pd-based organometallic thin films under the most common focused charged beams. The practical applications of combining spin-coated organometallic thin films with focused beam nanowriting in micro- and nano-lithography modern procedures are also discussed in this contribution.

Received 28th June 2024,
Accepted 13th September 2024

DOI: 10.1039/d4nr02680b

rsc.li/nanoscale

Introduction

Focused Ion Beam (FIB) technologies have been strongly developed in recent years to provide a rich palette of nanofabrication techniques. A roadmap of FIB has recently been published that comprises the great variety of applications under investigation.[1] One of the frequently used approaches in the topic is the combination of FIB with a precursor material that is delivered in gas phase to the area of interest by means of a gas injection system, which constitutes the backbone of the technique named Focused Ion Beam Induced Deposition (FIBID). FIBID is widely used in industry for transmission electron microscopy (TEM) lamellae preparation[2] and for circuit editing,[3] whereas research studies can benefit from FIBID for creating electrical contacts to individual micro/nano-structures,[4] for the growth of cantilever tips[5] and for the growth of nanopatterned materials such as magnetic ones,[6] with optical functionality,[7] or superconducting ones.[8] However, FIBID presents a serious drawback for certain applications due to the high ion doses required, which gives rise to long processing times and side effects in the deposit and substrate, such as ion-induced defects by implantation, amorphization or sputtering. These effects are more significant when heavy ions are used, such as Ga^+.[9] In order to mitigate this effect, the recent development of FIBID under cryogenic conditions (Cryo-FIBID, where a thin precursor layer is condensed on the substrate surface) has represented a step forward due to the decrease in the applied charge dose up to three orders of magnitude.[10] However, a cryogenic module[11] or a thermoelectric plate[12] is needed to lower the substrate temperature, and Cryo-FIBID cannot be as widely used as room-temperature FIBID despite its virtues.[13]

In order to take advantage of the FIB for the growth of functional nanostructures with low ion doses and without the need for resists, a different approach can be used. The method involves spin coating a solution of a precursor material containing the element that one targets to deposit on the substrate. Following this strategy, Au,[14] Ir,[15] and Pd structures[16] were grown in the past by Ga^+-FIB irradiation, but the low metal content in the resulting structure required a subsequent annealing process, thus limiting the range of applications and increasing the processing time. Recent work in our group

[a]*Instituto de Nanociencia y Materiales de Aragón (INMA), CSIC-Universidad de Zaragoza, 50018 Zaragoza, Spain. E-mail: deteresa@unizar.es*
[b]*Institute of Ion Beam Physics and Materials Research, Helmholtz-Zentrum Dresden-Rossendorf, 01328 Dresden, Germany*
[c]*Laboratorio de Microscopías Avanzadas, Universidad de Zaragoza, 50018 Zaragoza, Spain*

† Electronic supplementary information (ESI) available. See DOI: https://doi.org/10.1039/d4nr02680b

using this method, and palladium(II) acetate trimer (PdAc) as the starting precursor, has remarkably achieved the growth of functional Pd-rich (~50 at%) nanostructures without the need for any post-growth annealing step.[17] This work reports that structures with low electrical resistivity, ~70 μΩ cm, and high lateral resolution, 40 nm, are grown with ion beam doses that are very low, ~30 μC cm^{-2}. Thus, the process speed is comparable to that of standard electron beam lithography, which is used at the wafer level and has practical applications.[18] However, if these PdAc spin-coated films are irradiated by means of an electron beam, the required charge dose to achieve metallic structures is significantly higher.[19]

On the other hand, the use of FIB with sources of light ions (He^+ and Ne^+) has exhibited a better resolution for milling compared to standard Ga^+ sources,[20] due to their weaker interaction with matter as well as the small focused ion beam spots achievable, ~0.5 nm in the case of He^+ and ~2 nm in the case of Ne^+.[21] Both light ions are available in a commercial Helium Ion Microscope (HIM) that has been applied in recent years for precise FIB milling,[22–24] FIBID of functional materials with a high lateral resolution[25,26] and three-dimensional growth,[27,28] high-resolution and low-dose FIB lithography using resists[29,46] and local change in properties by means of FIB irradiation of catalytic,[44] magnetic,[30] electrical,[45] ferroelectric,[31] and superconducting properties.[32] Given this background, it is tempting to investigate the potential of the HIM for decomposing spin-coated PdAc films and compare the results with those previously obtained by means of Ga^+-FIB and electron irradiation. To the best of our knowledge, there are only a few examples in the literature where comparative studies about the effect of different beams on the same material, either for FIB milling[33–35] or for growing structures,[13] have been performed. Thus, the set of results presented in this contribution will be useful not only for the specific application investigated here, but also for a deeper understanding of the processes involved in the interaction between matter and charged particles as well as for aprioristic choices of the most suitable focused charged particle for a given application.

This contribution is organized as follows: (i) the initial sections describe the experiments in sequence: PdAc thin film preparation, irradiation by focused helium and neon beams and film thickness characterization, electrical characterization of the fabricated structures, and morphological and elemental composition analyses for the optimal conditions; (ii) the next section is dedicated to comparing the patterning of the electrical and structural properties of the formed Pd-based thin films after Ga^+, He^+, Ne^+ and electron irradiation; and (iii) in the last section of the article, we draw the main conclusions and discuss potential applications.

Results and discussion

PdAc thin film preparation procedure

The general procedure to fabricate the palladium-enriched nanofabricated structures (PdNSs) consists of three main steps (Fig. 1): (1) spin-coated Pd-based thin film fabrication, (2) irradiation of free design patterns by He^+/Ne^+ direct nanowriting, and (3) a washing step: removal of the non-exposed areas by immersing the sample in chloroform for a few seconds.

The preparation of Pd-based thin films, step 1, involves spreading 10 μL of a filtered $Pd_3(OAc)_6$ solution (0.1 M in $CHCl_3$) on pre-cleaned Si/SiO_2 substrates according to previously stated procedures.[14,15]

Irradiation by focused helium and neon nanobeams and film thickness characterization

Several spin-coated thin films were prepared in the same way for subsequent irradiation by means of a focused helium or neon beam. The initial thickness of these Pd-based thin films was measured by profilometry. Average thicknesses of 231.2 ± 11.8 nm and 234.4 ± 12.0 nm were obtained for the thin films subsequently irradiated by the He^+ and the Ne^+ beams, respectively. The helium irradiation was performed with an acceleration voltage of 30 kV, a gas pressure of 5×10^{-6} Torr, a beam-limiting aperture of 20 μm and a spot control set to 4.

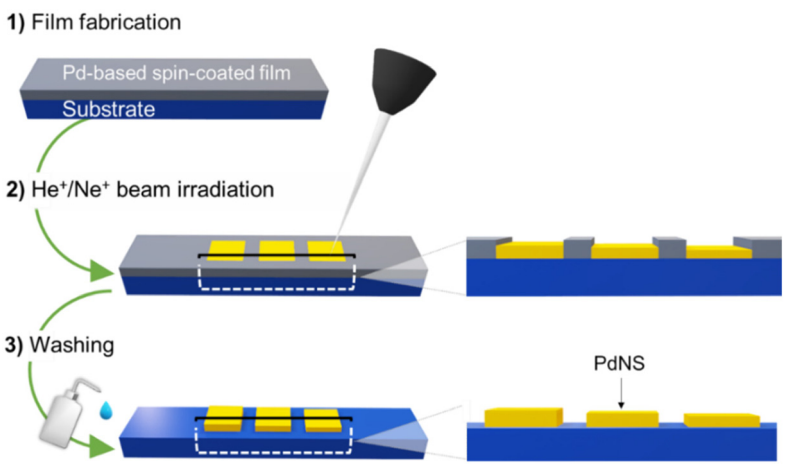

Fig. 1 Scheme for the fabrication of palladium-enriched metallic structures by direct focused He^+ and Ne^+ beam nanowriting.

The Ne^+ irradiation was performed by applying an acceleration voltage of 25 kV, a gas pressure of 2×10^{-6} Torr, and a beam-limiting aperture of 10 μm. This resulted in beam currents of approximately 1 pA and 8 pA for neon and helium nanowriting, respectively.

With regard to the He^+ irradiation conditions, a dose screening was carried out to establish a rough range of fluences by exposing one sample to fluences between 1 and 10 000 μC cm^{-2} (Fig. S1 in the ESI†). Once the effective range of irradiation doses was determined, Hall bar structures were fabricated at the selected fluences of 20, 40, 50, 60, 250, 500, 2500, 5000, 7500 and 10 000 μC cm^{-2} in order to study the electrical properties through a 4-microprobe station. In the case of Pd-based thin films exposed to Ne^+ irradiation, a control test was performed from 10 to 90 μC cm^{-2}. This range was then extended up to 1000 μC cm^{-2} where Hall bar structures were directly written to determine their electrical properties using fluences from 20 to 1000 μC cm^{-2}. The dependence of the thickness with increasing fluence for both types of irradiation is represented in Fig. 2.

The normalised thickness (t_n) is defined as the thickness or height of the resulting structure after the irradiation divided by the initial palladium acetate film thickness. The data used here to plot t_n were obtained from the AFM height measurement of the PdNSs after irradiation with a He^+ beam (4 different samples) and a Ne^+ beam (3 different samples). The initial thickness of the palladium acetate film was first measured for each sample using a profilometer. As shown in Fig. 2, in both cases, t_n is dependent on the fluence applied. The film areas irradiated with a helium fluence lower than 10 μC cm^{-2} were removed during the washing step (step 3, Fig. 1), meaning that the applied fluence was not sufficient to decompose the film and subsequently to change the film solubility. For neon irradiation, PdNSs remained after the washing step. The data obtained indicate that for fluences up to 34 μC cm^{-2} and 120 μC cm^{-2} for He^+ and Ne^+ irradiation, respectively, there is an increase in t_n as the applied dose is increased. This is mainly due to the decomposition of the initial Pd-based thin film and due to a decrease in the solubility of the irradiated parts of the film, which behaves similarly to a negative photoresist.[16] After these maxima, t_n decreases as fluences increase. This thickness decrease can be associated with the disappearance of the soluble species and the corresponding formation of more compact structures. When applying He^+ irradiation greater than ~200 μC cm^{-2}, the rate of thickness decrease with fluence slows down and reaches an almost constant value of t_n, independent of the applied fluence, suggesting that the maximum film decomposition has been achieved. In the case of neon irradiation, fluences above 1000 μC cm^{-2} have not been applied in order to find a constant t_n value. This was decided on the basis of the plot trend shown in Fig. 2b; it was considered that an increase in fluence would not result in a significant improvement in resistivity.

A similar methodology was previously applied by us to fabricate PdNSs using both a focused electron beam[19] and a focused gallium beam.[17] Nevertheless, these studies did not include any indication as to whether or not the removal step of the non-irradiated material had any effect on the thickness. This point was therefore here investigated by first measuring the shrinkage of the thin film after irradiation and before immersing the sample in chloroform.

With this aim, AFM images were registered immediately after the direct writing process without any further action (see step 2, Fig. 1), as shown in Fig. 3 – left. The sample was then immersed in the solvent, fresh $CHCl_3$ (step 3, Fig. 1), and the topography of the as-fabricated structures was re-registered, as shown in Fig. 3, right. Here, there is a representative example of the procedure followed.

This control experiment was investigated for one of the samples studied, which was exposed to the He^+ beam and had an initial film thickness of 221.4 ± 2.5 nm, measured by profilometry. The film shrinkage after the He^+ irradiation, but before the washing step, and the thickness of the resulting structure after the washing step, have been extracted from the corresponding AFM line profiles (blue lines, Fig. 3, top). The sum of both values must be close to the initial film thickness. For instance, in Fig. 3, these values are highlighted for a fluence of 30 μC cm^{-2}, the film shrinkage being 64.5 nm, and

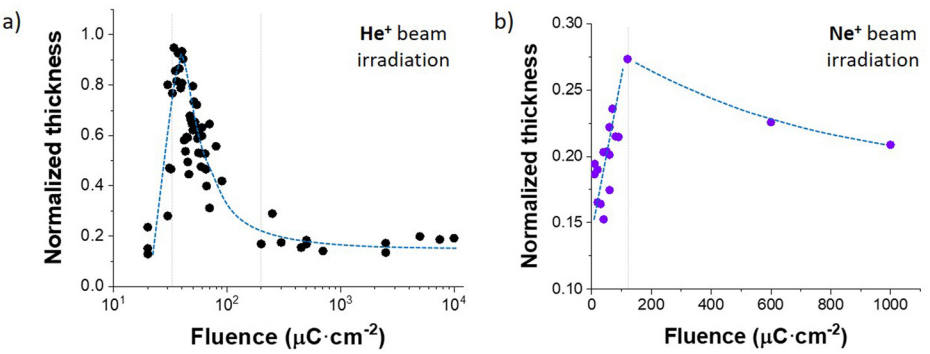

Fig. 2 Normalized PdNSs thicknesses after removal of the non-exposed areas *versus* the applied ion fluence. (a) Fabricated by He^+ direct-writing and (b) by Ne^+ direct-writing. Data are normalized with respect to the as-prepared film thickness. To clarify the plot trends, a blue dotted line has been added.

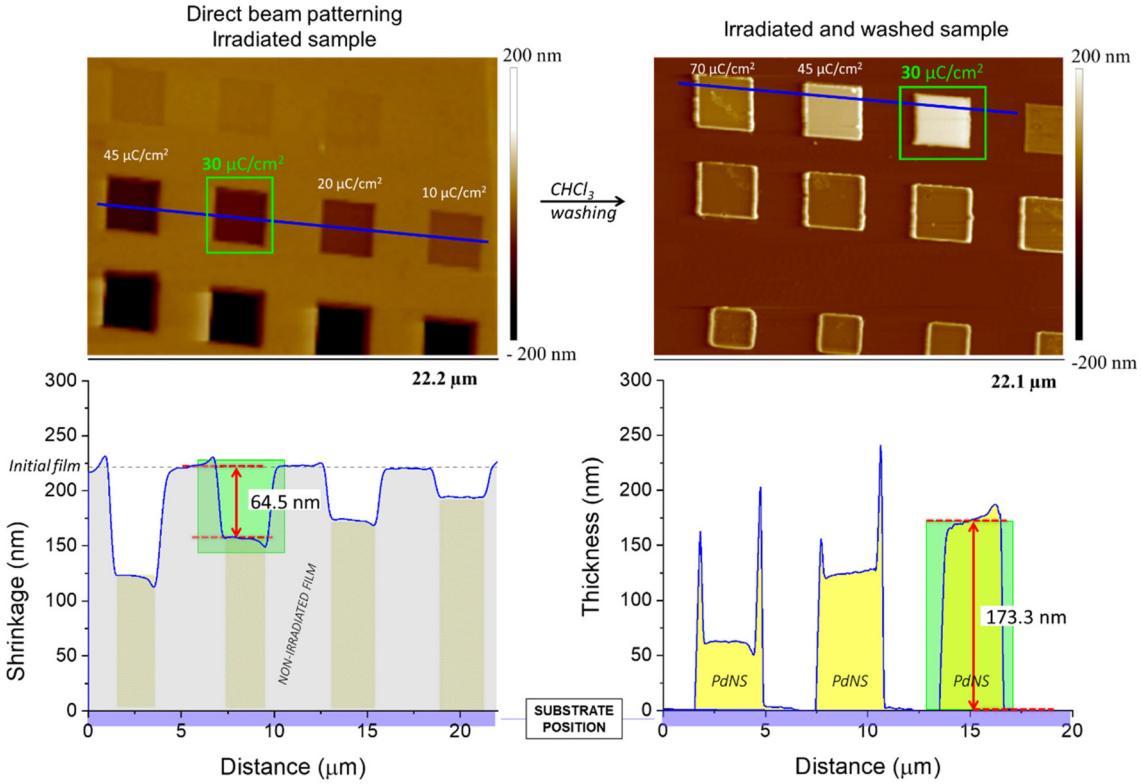

Fig. 3 Top: AFM images recorded after direct He^+ beam irradiation, before (left) and after (right) immersion in $CHCl_3$ to remove the non-irradiated areas – top views of the sample. Bottom: registered profiles for the blue lines on the corresponding upper images. The purple rectangle at the bottom of the figure, represents the position of the substrate; it has been added to facilitate interpretation.

the resulting structure thickness being 173.3 nm. The sum of these two values is 237.8 nm, which is close to the initial value of the film measured by profilometry (we compared the values registered by different characterization techniques).

The same test was applied for different doses. All the measurements are summarized in Fig. S2.† These results confirm that the washing step has negligible influence on the thickness of the PdNSs fabricated by the nanowriting procedure.

Electrical characterization of the fabricated structures

In order to determine the electrical properties of the PdNSs, patterns in the shape of Hall bars were directly written at the selected fluences. The current *versus* voltage (*I–V*) curves were subsequently recorded at room temperature by means of a four-probe station placed inside the HIM chamber, Fig. 4a. In Fig. 4b, left, the linear *I–V* curves recorded from the structures made by He^+ irradiation using fluences above 250 μC cm^{-2} are shown. These results demonstrate the ohmic behaviour expected for metallic structures. The structures produced at fluences below this threshold were not measurable. In the case of the structures fabricated by Ne^+ irradiation, a linear *I–V* response was observed in all cases, as shown in Fig. 4c, left.

The resistivity values *versus* the applied dose plotted for He^+ and Ne^+ irradiation, respectively, on the right-hand side of Fig. 4b and c have been calculated after precisely measuring the geometric dimensions of each structure, by AFM (*z* dimension) and HIM or SEM images (*x* and *y* dimensions). In both cases, it is observed that the resistivity decreases as a function of the applied dose, reaching almost constant values for the highest doses. Specifically, a resistivity value of ~152 μΩ cm is attained with He^+ fluences of 5000 μC cm^{-2}, while a value of ~141 μΩ cm is reached with Ne^+ fluences of 1000 μC cm^{-2}. These have been set as optimal irradiation fluences. Note that for He^+ irradiation, the resistivity decreases only slightly upon increasing the fluence over 5000 μC cm^{-2}. A straightforward comparison can be performed between the He^+ irradiation and the Ne^+ irradiation: the Ne^+ irradiation is more efficient in film decomposition, as expected, given its larger mass and, as a consequence, its larger linear momentum ($p = m \cdot v$), for the applied accelerating voltage. A larger linear momentum implies, in principle, a higher capacity for atom displacement and bond breaking. However, the mechanism of the film decomposition by ion irradiation is complex,[36,37] as simulations for Ga^+ irradiation showed in the past,[17] and other effects such as preferential sputtering or heating effects could also contribute at large irradiation doses.

Morphological and elemental composition analyses for the optimal conditions of ion irradiation

In order to correlate the electrical properties with morphological composition and elemental composition, cross-sectional lamellae were extracted from such structures fabricated with the optimal He^+ and Ne^+ fluences and analysed by means of

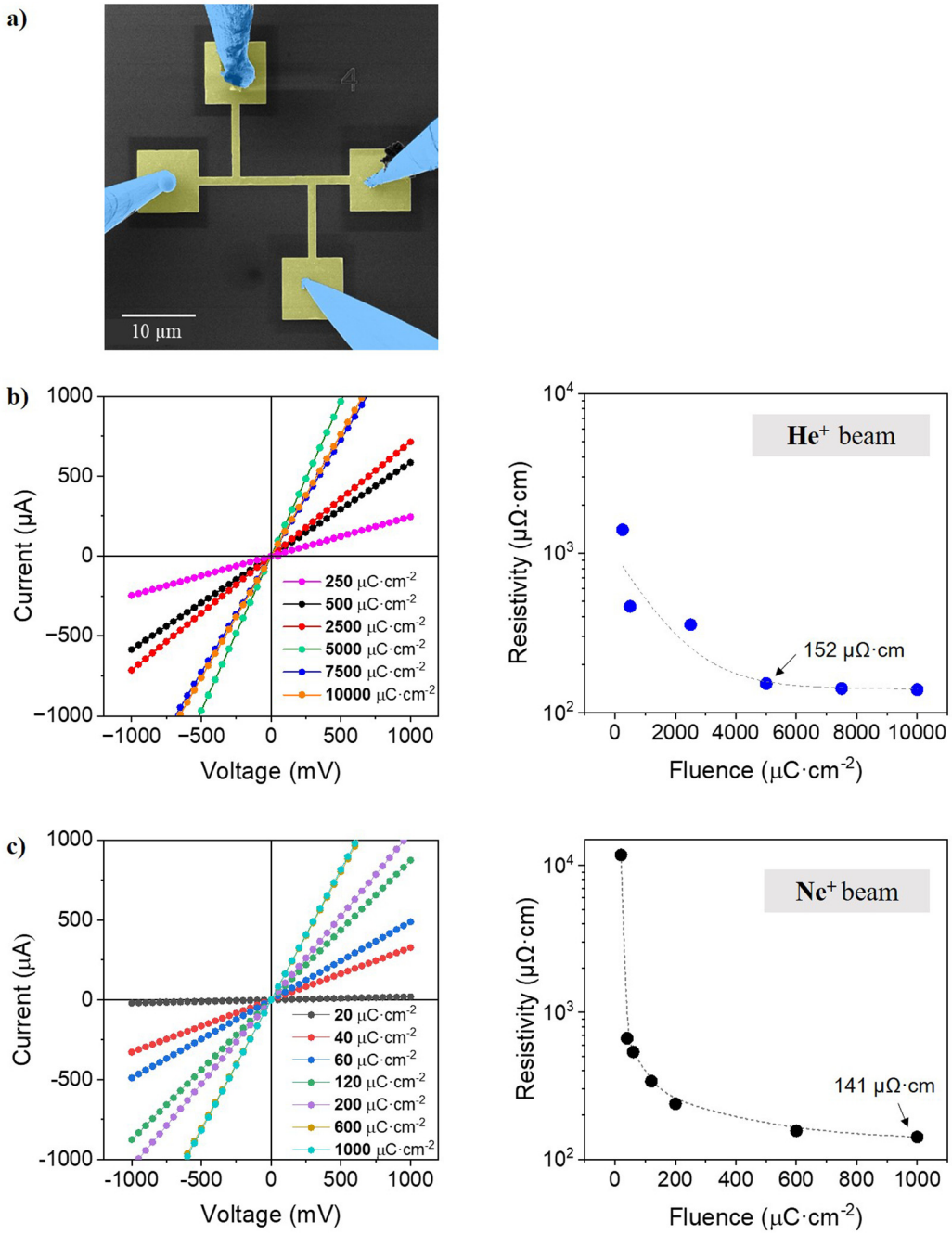

Fig. 4 (a) HIM image of one of the measured Hall bars by using a 4-probe technique. The image has been artificially coloured for clarity: blue = microprobes, yellow = Pd-enriched structure. (b) Electrical properties corresponding to the Pd structures fabricated by focused helium beam direct writing. Left: *I*–*V* curves for the PdNSs fabricated using the indicated fluences . Right: electrical resistivity of the Pd structures as a function of the applied fluences. (c) Electrical properties corresponding to the Pd structures fabricated by focused neon beam direct writing. Left: *I*–*V* curves for the PdNSs fabricated using the indicated fluences. Right: electrical resistivity of the Pd structures as a function of the applied fluences.

TEM techniques. Fig. S3† shows the HAADF images and EDS results using the STEM mode for the two of them (5000 μC cm^{-2} and 1000 μC cm^{-2}, respectively), demonstrating that the fabricated structures have in both cases an atomic palladium content of *ca.* 36%. Interestingly, Ne^+ irradiation at a lower dose compared to He^+ seems to produce higher agglomeration in the internal structure and a lower number of grain boundaries, which is the natural explanation for its slightly lower resistivity despite the same Pd content found.

Comparison of the patterning of the studied Pd-based thin films under Ga^+, He^+, Ne^+ and electron beams

As already mentioned, similar Pd-based films were previously fabricated by direct nanowriting through focused gallium and

electron beams.[17,19] In order to put all the results in context, Fig. 5 illustrates a comparison of applying Ga^+-, Ne^+-, He^+- and electron-focused beams to decompose a palladium spin-coated film with the aim of obtaining a metallic structure. In this figure, the following physical properties are compared: resistivity, composition and grain size.

Fig. 5a shows how the PdNS resistivity decreases as the fluence increases for all kinds of focused beam irradiation. A quick look at this plot shows that the Ne^+ and He^+ beams achieve the lowest resistivities using doses between those required for Ga^+ and electron beams. In fact, the lowest resistivity value, ~70 μΩ cm, was achieved under Ga^+ irradiation using a fluence as low as 30 μC cm^{-2}, while resistivity values of 141, 152 and 145 μΩ cm were obtained under Ne^+, He^+ and electron irradiation using fluences of 1000, 5000 and 30 000 μC cm^{-2}, respectively. One can compare these optimal conditions to produce conductive Pd nanostructures in terms of elemental quantification and morphological analyses of the corresponding cross-sections. On the one hand, as shown in the bar chart, Fig. 5c, the Pd content of the Ga^+-fabricated structures was significantly higher (~56 at%) compared to the structures grown through Ne^+, He^+ and electron irradiation (~36 at%), providing an explanation for its significantly lower resistivity value. On the other hand, Fig. 5b illustrates the cross-sectional TEM images of these PdNSs, where slight differences in the grain size can be observed that can be attributed to the specific charged particle used. No unwanted damage caused by the ion irradiation has been observed. The presence of grain boundaries is well known to increase the electrical resistivity and might explain the slight differences in the resistivity for the Ne^+, He^+ and electron irradiation, which show small differences in resistivity despite having the same Pd content.

In order to put the obtained results in context, in Fig. 6, we represent the values of resistivity and charge dose required for the growth, under optimal conditions, of the PdNSs using the four beams as well as the corresponding values of related growth techniques.

In particular, we have selected the growth of W and of Co by FEBID and FIBID, as well as the growth of W and of Co by

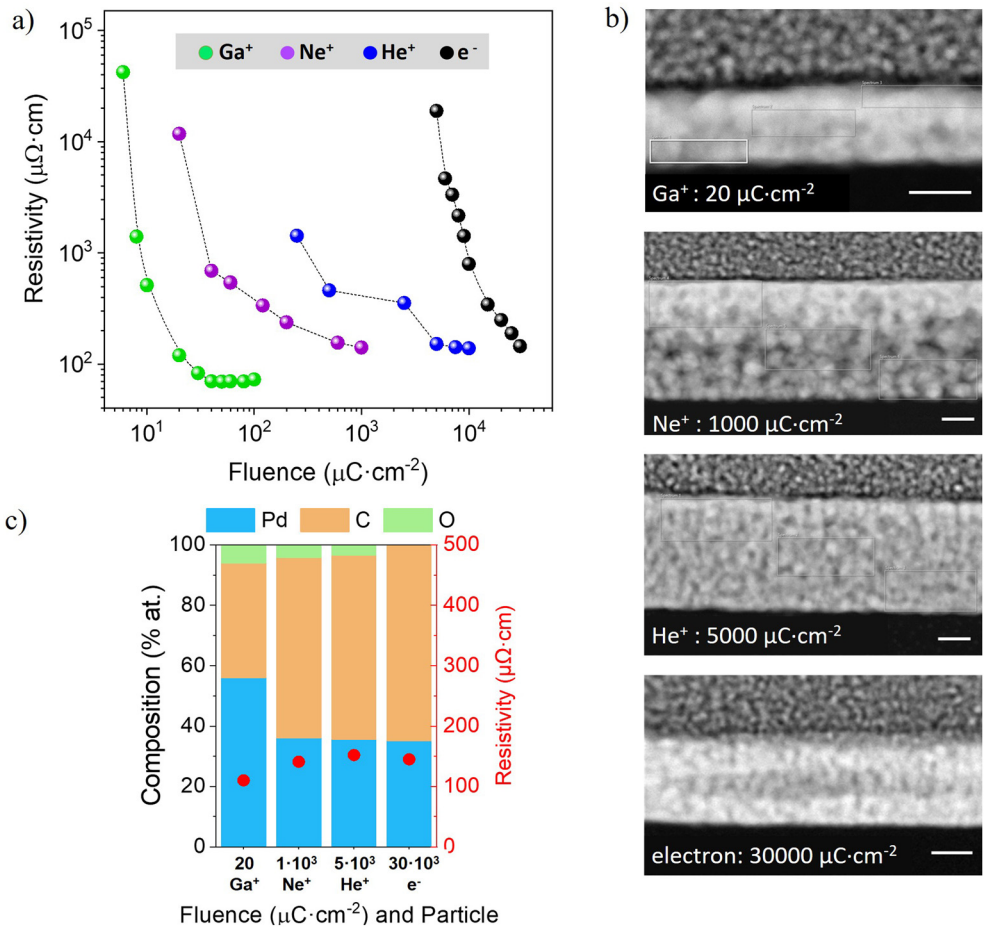

Fig. 5 (a) Comparative plot of the resistivity as a function of the applied fluence for the four different charged-particle beams used for the PdAc film decomposition. (b) Cross-sectional STEM-HAADF images for PdNSs fabricated by irradiation with the indicated beam and fluence. The scale bar for all images is 10 nm.. (c) Comparative elemental quantification (% atomic content) of Pd, C and O determined for PdNSs fabricated by irradiation with the indicated beam and fluence.. The scale bar for all images is 10 nm.

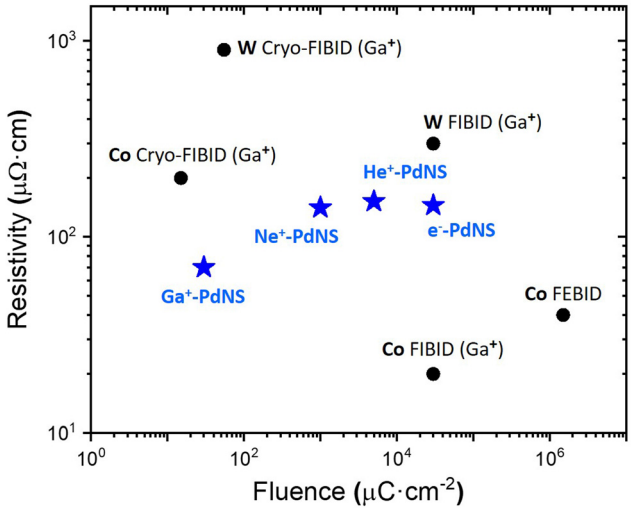

Fig. 6 Resistivity values *versus* the applied fluence for other FIBID/FEBID techniques and materials, compared to the palladium-enriched nanofabricated structures (PdNSs). Ga^+-PdNS, e^--PdNS and black data points have been obtained from ref. 10, 11, 17 and 19.

Cryo-FIBID.[10] One can see in Fig. 6 that Co can be grown by FEBID and FIBID, producing very low resistivity (~20 μΩ cm for Co by FIBID), but unfortunately, the charge dose required is so high that these processes should be limited to structures of very small dimensions. The growth of W by FIBID suffers from the same problem of the high charge dose required and, additionally, the obtained resistivity still corresponds to metallic values, but is ten times higher than that for Co grown by FIBID. Regarding the charge dose, the use of Cryo-FIBID is very convenient, because W can be deposited with 50 μC cm^{-2}, whereas Co can be deposited with 15 μC cm^{-2}. However, the resistivity values of these deposits, despite being metallic, are above 200 μΩ cm. In the case of the PdNSs, the use of Ga^+ is indeed very competitive in terms of both the low charge dose required (30 μC cm^{-2}) and the low resistivity attained (~70 μΩ cm). Therefore, it emerges as a clear choice for applications where fast growth and low resistivity are required. As will be discussed later in the Outlook section, the growth of PdNSs by Ne^+ and He^+ irradiation would be justified if, in future, a higher lateral resolution than that in the case of Ga^+ is achieved, or if Ga^+ produces unwanted damage in the surrounding materials.

Materials and methods

Spin coated films were fabricated using a Süss Microtech spin coater, placed inside an ISO5 clean room. The powder compound $Pd_3(OAc)_6$ was purchased and used as received. $CHCl_3$, CromAR® HPLC, was used as a solvent to prepare the films and to remove the non-irradiated areas. Initial film thicknesses were determined by profilometry using KLA-Tencor P6 equipment.

An UltraObjective AFM from SIS attached to an Olympus BX51 optical microscope was used to register the depth profile of the irradiated areas before removal of the non-irradiated ones, and to measure the height of the final structures.

A Zeiss ORION NanoFab helium ion microscope (HIM)[21] was used for irradiation of the films. The machine is equipped with 4 Kleindiek MM3A manipulators for *in situ* electrical probing, a home built and commercially available time-of-flight secondary ion mass spectrometer (TOF-SIMS) and a heating stage. The NPVE patterning software and pattern generator from FIBICS were used to write the patterns.

Current *versus* voltage (*I*–*V*) curves were registered using a four-probe station inside the HIM, at room temperature. A Keithley Instruments 2614B source meter unit was connected *via* a chamber feedthrough using tri-ax shielded cables. Hall bar-like geometries were used to perform the measurements. To determine the resistivity value for each applied fluence, the dimensions of the directly written Hall bars were measured by using a SEM Quanta FEG 250 and an AFM.

Lamellae from PdNSs directly written onto Si/SiO_2 substrates were fabricated using a Helios Nanolab 650 dual beam microscope and attached to a TEM copper grid. Energy-dispersive X-ray spectroscopy (EDS) with an energy of resolution ~125 eV and high-angle annular dark-field (HAADF) imaging at 300 keV were performed by transmission electron microscopy (TEM) using an analytical Titan low-base instrument.

Conclusions and outlook

Conclusions

In the present article, optimization of the decomposition of PdAc spin-coated films by means of irradiation with He^+ and Ne^+ focused beams has been presented. It has been observed that for both beams, it is possible to achieve metallic structures with a Pd atomic content of ~36%. The use of Ne^+ is more efficient, with a required fluence of 1000 μC cm^{-2}, compared to 5000 μC cm^{-2} in the case of He^+ irradiation. This behavior is intermediate between that of Ga^+ irradiation (required fluence of 30 μC cm^{-2}) and that of electron irradiation (required fluence of 30 000 μC cm^{-2}), strongly suggesting the important role played by the mass and the linear momentum of the beam particle in the efficiency of the decomposition. Moreover, the comparison among the four beams indicates that the use of Ga^+ irradiation is most suitable when the lowest resistivity is required and, in addition, it gives hints to improve the process in terms of fluence and resistivity by using even heavier ions than Ga^+, such as Xe^+,[38] Rb^+,[39] Au^+,[40] *etc*. However, the damage created by heavy ions in the surrounding materials should be a factor to consider in the choice of the ion.

Compared to resist-based lithography techniques such as electron beam lithography (EBL), which have multiple steps and require multiple pieces of equipment, direct-writing tech-

niques such as those represented in Fig. 6 (black dots), stand out for consisting of a single lithography step. However, they present disadvantages such as the availability of only a few precursor materials and, in the case of FEBID and FIBID, also the high fluence needed. This means that FEBID and FIBID are time-consuming and their scalability is limited. Cryo-FIBID is a much faster growth technique, but this technique calls for cryogenic temperatures and has the difficulty that the precursor is only condensed on a limited area, and so it is not so implementable in terms of upscaling and process compatibility. However, the decomposition of organometallic spin-coated films by charged-particle beams could gather the virtues of all the previous techniques. Given the high fluence needed, the technique is not so interesting in the case of electron or He^+ irradiation, which implies a high processing time, but the technique is competitive in the case of Ne^+ irradiation and definitely very competitive in the case of Ga^+ irradiation due to the very low irradiation dose required (30 μC cm^{-2}). If one compares it to the typical fluences used for resist exposure in EBL, which depend on the specific resist but are typically in the range of a few hundred μCcm^{-2},[41] it can be stated that the fluence required for the ion decomposition of organometallic spin-coated films should not be an impediment for its upscaling and their use at the wafer level. Let us highlight that the Pd-enriched structures created by means of this methodology are readily functional (metallic behaviour) and do not need any post-treatment or annealing steps.

Outlook

It is also worth discussing other virtues of the decomposition of organometallic spin-coated films, such as the tunability of the electrical resistivity with the fluence and the type of ion used. Given the broad range of resistivities obtained depending on the fluence and the charged particle used, it is possible to fabricate structures with spatially dependent resistivity, which could find application in functional devices. As an example, our group has recently achieved the fabrication of electrical gate contacts through the combination of irradiation on PdAc films by focused electron and Ga^+ beams, so that insulating and metallic behaviors are respectively achieved on the same device depending on the type of irradiation (Salvador-Porroche *et al.*, manuscript under review). With regard to the resolution of the patterns, in previous work, we were able to obtain gaps of 40 nm by means of focused Ga^+ irradiation of PdAc films.[17] One could expect a better resolution in the case of focused Ne^+ and He^+ irradiation, given their smaller ion beam spot and the lower interaction volume near the surface. Our preliminary tests have not been successful, given the use of relatively thick PdAc films >200 nm. These tests, however, suggested that by using thinner films, it could be possible to attain a higher resolution. The technical problem is similar to the case of negative-resist-based lithography and requires a thorough optimization study that is beyond the aim of the current study.[42]

In previous paragraphs, we have discussed the virtues of using organometallic spin-coated films and charge-particle irradiation for lithography, such as its single-step nature, the low fluence required that allows process upscaling, and the low resistivity achievable, as well as the disadvantages, such as the need for exploration of more organometallic precursors that could be used in this process. With the available data, nevertheless, it is possible to put forward some potential applications of the technique. The metallic nature of the Pd-enriched structures created by focused Ga^+, Ne^+ and He^+ irradiation of PdAc allows for the *in situ* growth of metallic contacts in a single step and at high speed.[17] This procedure could be preferred for standard FEBID and FIBID growth when the area of the metallic contacts is large (and time is an issue) or when the metallic contacts have to be repeated multiple times. Besides, the use of PdAc spin-coated films might be useful in those cases where the resists used in EBL contaminate the surface and modify the properties of the functional material.[43] Moreover, given the metallic nature of the Pd-enriched structures, they could be used to provide conductivity for insulating and transparent films and devices that are used in optoelectronic applications, as we showed by means of focused Ga^+ irradiation of PdAc films.[17] Last, but not least, the use of other organometallic spin-coated films based on other functional elements beyond Pd could open the route to applications in other domains such as magnetism, superconductivity, nano-optics, catalysis, *etc.*, and we are already exploring some of them.

Author contributions

L. H. contributed to the idea, fabricated the samples, participated in the irradiation and electrical measurements, performed the data handling and characterization, participated in the interpretation, and drafted the manuscript. A. S.-P. contributed to the idea and contributed to the interpretation and data comparison. G. H. directed and performed the irradiation and electrical measurements using the HIM. P. C. contributed to the idea and supervised the project. J. M. D. T. conceived the idea, supervised the project, participated in the interpretation and drafted the manuscript. All authors approved the final version of the manuscript.

Data availability

Data for this article, including the raw data of current *versus* voltage, are available at Zenodo at **https://doi.org/10.5281/zenodo.12580763**.

Conflicts of interest

The authors declare no conflict of interest.

Acknowledgements

The authors are thankful for the financial support from the Gobierno de Aragón through the grant numbers E13_23R and E31_23R, for the financial support from the grants PID2020-11223914RB-I00, PID2022-141433OB-I00 PDC2023-145810-I00, PID2023-146451OB-I00, RED2022-134096-T and TED2021-131318B-I00 funded by MCIN/AEI/10.13039/501100011033 and the European Union "NextGenerationEU"/PRTR. This research work has also been funded by the European Commission – NextGenerationEU (Regulation EU 2020/2094), through CSIC's Quantum Technologies Platform (QTEP). The authors acknowledge the use of the facilities as well as the technical advice provided by the National Facility ELECMI ICTS, node "Laboratorio de Microscopias Avanzadas (LMA)" at "Universidad de Zaragoza", and thefinancial support through a short-term scientific mission funded by the COST Action CA19140 – Focused Ion Technology for Nanomaterials, supported by COST (European Cooperation in Science and Technology) – **https://www.fit4nano.eu/**.

References

1 K. Höflich, G. Hobler, F. I. Allen, T. Wirtz, G. Rius, L. McElwee-White, A. V. Krasheninnikov, M. Schmidt, I. Utke, N. Klingner, M. Osenberg, R. Córdoba, F. Djurabekova, I. Manke, P. Moll, M. Manoccio, J. M. De Teresa, L. Bischoff, J. Michler, O. De Castro, A. Delobbe, P. Dunne, O. V. Dobrovolskiy, N. Frese, A. Gölzhäuser, P. Mazarov, D. Koelle, W. Möller, F. Pérez-Murano, P. Philipp, F. Vollnhals and G. Hlawacek, *Appl. Phys. Rev.*, 2023, **10**, 41311.

2 J. Mayer, L. A. Giannuzzi, T. Kamino and J. Michael, *MRS Bull.*, 2007, **32**, 400–407.

3 H. Wu, D. Ferranti and L. Stern, *Microelectron. Reliab.*, 2014, **54**, 1779–1784.

4 K. Gross, J. J. P. Barragán, S. Sangiao, J. M. De Teresa, L. Lajaunie, R. Arenal, H. A. Calderón and P. Prieto, *Nanotechnology*, 2016, **27**, 365708.

5 F. I. Allen, J. M. De Teresa and B. Onoa, *ACS Appl. Mater. Interfaces*, 2024, **16**, 4439–4448.

6 M. Gabureac, L. Bernau, I. Utke and G. Boero, *Nanotechnology*, 2010, **21**, 115503.

7 M. Esposito, V. Tasco, F. Todisco, M. Cuscunà, A. Benedetti, D. Sanvitto and A. Passaseo, *Nat. Commun.*, 2015, **6**, 6484.

8 F. Sigloch, S. Sangiao, P. Orús and J. M. de Teresa, *Nanoscale Adv.*, 2022, **4**, 4628–4634.

9 L. Bruchhaus, P. Mazarov, L. Bischoff, J. Gierak, A. D. Wieck and H. Hövel, *Appl. Phys. Rev.*, 2017, **4**, 011302.

10 A. Salvador-Porroche, S. Sangiao, C. Magén, M. Barrado, P. Philipp, D. Belotcerkovtceva, M. V. Kamalakar, P. Cea and J. M. De Teresa, *Nanoscale Adv.*, 2021, **3**, 5656–5662.

11 R. Córdoba, P. Orús, S. Strohauer, T. E. Torres and J. M. De Teresa, *Sci. Rep.*, 2019, **9**, 14076.

12 P. Orús, F. Sigloch, S. Sangiao and J. M. De Teresa, *Appl. Sci.*, 2021, **11**, 10123.

13 J. M. De Teresa, P. Orús, R. Córdoba and P. Philipp, *Micromachines*, 2019, **10**, 799.

14 P. Hoffmann, G. Ben Assayag, J. Gierak, J. Flicstein, M. Maar-Stumm and H. van den Bergh, *J. Appl. Phys.*, 1993, **74**, 7588–7591.

15 P. Hoffmann, H. van den Bergh, J. Flicstein, G. Ben Assayag, J. Gierak and J.-F. Bresse, *J. Vac. Sci. Technol., B: Microelectron. Nanometer Struct.–Process., Meas., Phenom.*, 1991, **9**, 3483–3486.

16 M. E. Gross, W. L. Brown, L. R. Harriott, K. D. Cummings, J. Linnros and H. Funsten, *J. Appl. Phys.*, 1989, **66**, 1403–1410.

17 A. Salvador-Porroche, L. Herrer, S. Sangiao, P. Philipp, P. Cea and J. M. De Teresa, *ACS Appl. Mater. Interfaces*, 2022, **14**, 28211–28220.

18 Y. Chen, *Microelectron. Eng.*, 2015, **135**, 57–72.

19 A. Salvador-Porroche, L. Herrer, S. Sangiao, J. M. De Teresa and P. Cea, *Nanotechnology*, 2022, **33**, 405302.

20 M. Melli, A. Polyakov, D. Gargas, C. Huynh, L. Scipioni, W. Bao, D. F. Ogletree, P. J. Schuck, S. Cabrini and A. Weber-Bargioni, *Nano Lett.*, 2013, **13**, 2687–2691.

21 G. Hlawacek, V. Veligura, R. van Gastel and B. Poelsema, *J. Vac. Sci. Technol., B: Nanotechnol. Microelectron.: Mater., Process., Meas., Phenom.*, 2014, **32**, 020801.

22 H. Kollmann, X. Piao, M. Esmann, S. F. Becker, D. Hou, C. Huynh, L. O. Kautschor, G. Bösker, H. Vieker, A. Beyer, A. Gölzhäuser, N. Park, R. Vogelgesang, M. Silies and C. Lienau, *Nano Lett.*, 2014, **14**, 4778–4784.

23 D. Emmrich, A. Beyer, A. Nadzeyka, S. Bauerdick, J. C. Meyer, J. Kotakoski and A. Gölzhäuser, *Appl. Phys. Lett.*, 2016, **108**, 163103.

24 M. C. Lemme, D. C. Bell, J. R. Williams, L. A. Stern, B. W. H. Baugher, P. Jarillo-Herrero and C. M. Marcus, *ACS Nano*, 2009, **3**, 2674–2676.

25 H. Wu, L. A. Stern, D. Xia, D. Ferranti, B. Thompson, K. L. Klein, C. M. Gonzalez and P. D. Rack, *J. Mater. Sci.: Mater. Electron.*, 2014, **25**, 587–595.

26 P. Orús, R. Córdoba, G. Hlawacek and J. M. De Teresa, *Nanotechnology*, 2021, **32**, 085301.

27 R. Córdoba, D. Mailly, R. O. Rezaev, E. I. Smirnova, O. G. Schmidt, V. M. Fomin, U. Zeitler, I. Guillamón, H. Suderow and J. M. De Teresa, *Nano Lett.*, 2019, **19**, 8597–8604.

28 A. Belianinov, M. J. Burch, A. Ievlev, S. Kim, M. G. Stanford, K. Mahady, B. B. Lewis, J. D. Fowlkes, P. D. Rack and O. S. Ovchinnikova, *Micromachines*, 2020, **11**, 527.

29 V. Sidorkin, E. van Veldhoven, E. van der Drift, P. Alkemade, H. Salemink and D. Maas, *J. Vac. Sci. Technol., B: Microelectron. Nanometer Struct.–Process., Meas., Phenom.*, 2009, **27**, L18–L20.

30 H. Cansever, M. S. Anwar, S. Stienen, K. Lenz, R. Narkowicz, G. Hlawacek, K. Potzger, O. Hellwig, J. Fassbender, J. Lindner and R. Bali, *Sci. Rep.*, 2022, **12**, 14809.

31 S. Saremi, R. Xu, F. I. Allen, J. Maher, J. C. Agar, R. Gao, P. Hosemann and L. W. Martin, *Phys. Rev. Mater.*, 2018, **2**, 084414.
32 S. A. Cybart, E. Y. Cho, T. J. Wong, B. H. Wehlin, M. K. Ma, C. Huynh and R. C. Dynes, *Nat. Nanotechnol.*, 2015, **10**, 598–602.
33 S. Jiang and V. Ortalan, *Nanomaterials*, 2023, **13**, 2898.
34 E. I. Preiß, B. Merle, Y. Xiao, F. Gannott, J. P. Liebig, J. M. Wheeler and M. Göken, *J. Mater. Res.*, 2021, **36**, 2505–2514.
35 F. I. Allen, N. R. Velez, R. C. Thayer, N. H. Patel, M. A. Jones, G. F. Meyers and A. M. Minor, *Nanoscale*, 2019, **11**, 1403–1409.
36 S. Indrajith, P. Rousseau, B. A. Huber, C. Nicolafrancesco, A. Domaracka, K. Grygoryeva, P. Nag, B. Sedmidubská, J. Fedor and J. Kočišek, *J. Phys. Chem. C*, 2019, **123**, 10639–10645.
37 E. Bilgilisoy, R. M. Thorman, M. S. Barclay, H. Marbach and D. H. Fairbrother, *J. Phys. Chem. C*, 2021, **125**, 17749–17760.
38 C. Rue and B. Carrigan, *ISTFA* 2012, 2012, 447–454.
39 Y. Li, S. Xu, M. Sezen, F. Bakan Misirlioglu and E. J. D. Vredenbregt, *J. Vac. Sci. Technol., B: Nanotechnol. Microelectron.: Mater., Process., Meas., Phenom.*, 2023, **41**, 042803.
40 J. Gierak, A. Madouri, E. Bourhis, L. Travers, D. Lucot and J. C. Harmand, *Microelectron. Eng.*, 2010, **87**, 1386–1390.
41 A. E. Grigorescu and C. W. Hagen, *Nanotechnology*, 2009, **20**, 292001.
42 H. Duan, D. Winston, J. K. W. Yang, B. M. Cord, V. R. Manfrinato and K. K. Berggren, *J. Vac. Sci. Technol., B: Nanotechnol. Microelectron.: Mater., Process., Meas., Phenom.*, 2010, **28**, C6C58–C6C62.
43 J. Fan, J. M. Michalik, L. Casado, S. Roddaro, M. R. Ibarra and J. M. De Teresa, *Solid State Commun.*, 2011, **151**, 1574–1578.
44 E. Mitterreiter, Y. Liang, M. Golibrzuch, D. McLaughlin, C. Csoklich, J. D. Bartl, A. Holleitner, U. Wurstbauer and S. Bandarenka, In-situ visualization of hydrogen evolution sites on helium ion treated molybdenum dichalcogenides under reaction conditions, *npj 2D Materials and Applications*, 2019, **3**(25).
45 D. S. Fox, Y. Zhou, P. Maguire, A. O'Neil, C. Ó 'Coileain, R. Gatensby, A. M. Glushenkov, Tao Tao, G. S. Duesberg, I. V. Shvets, M. Abid, M. Abid, H.-C. Wu, Ying Chen, J. N. Coleman, J. F. Donegan and Hongzhou Zhang, Nanopatterning and Electrical Tuning of MoS2 Layers with a Subnanometer Helium Ion Beam, *Nano Lett*, 2015, **15**, 5307–5313.
46 D. Winston, V. R. Manfrinato, S. L. Nicaise, L. L. Cheong, H. Duan, D. Ferranti, J. Marshman, S. McVey, L. Stern, J. Notte and K. K. Bergreen, Neon Ion Beam Lithography (NIBL), *Nano Lett.*, 2011, **11**(10), 4343–4347.